RSC Advances

PAPER

View Article Online
View Journal | View Issue

Open Access Article. Published on 26 October 2023. Downloaded on 10/1/2024 11:16:26 AM.
This article is licensed under a Creative Commons Attribution-NonCommercial 3.0 Unported Licence.

Check for updates

Cite this: *RSC Adv.*, 2023, **13**, 31027

# Processing on crystal growth, structure, thermal property, and nuclear magnetic resonance of organic–inorganic hybrid perovskite type $[NH_3(CH_2)_6NH_3]ZnCl_4$ crystal†

Ae Ran Lim *[ab] and Sun Ha Kim[cd]

Received 23rd August 2023
Accepted 2nd October 2023

DOI: 10.1039/d3ra05752f

rsc.li/rsc-advances

Organic–inorganic hybrid compounds have recently gained significant attention in recent years due to their diverse applications. Herein, $[NH_3(CH_2)_6NH_3]ZnCl_4$ crystals were grown, and their triclinic structure, phase transition temperature ($T_C$ = 408 K), and high thermal stability ($T_d$ = 584 K) was determined using X-ray diffraction (XRD), differential scanning calorimetry, and thermogravimetry measurements. By analyzing the chemical in response to temperature changes, we observed that the coordination geometry around $^1H$ and $^{13}C$ were highly symmetric below $T_C$, whereas their symmetry was lowered above $T_C$. The change of N–H···Cl hydrogen bond from XRD results and the change of $^{14}N$ NMR chemical shifts was due to the changes to the coordination geometry of $Cl^-$ around $Zn^{2+}$ in the $ZnCl_4$ anion. The activation energy of $^1H$ was three times greater than that of $^{13}C$, and this result indicates that the energy transfer of $^{13}C$ was easier than those of $^1H$. We compared the results for $[NH_3(CH_2)_nNH_3]ZnCl_4$ ($n$ = 6) studied here with those for $n$ = 2, 3, 4, and 5 obtained from previous studies. The characteristics of the length of $CH_2$ in the methylene chain are expected to be used for potential applications in the near future.

## 1. Introduction

The research on organic–inorganic hybrid compounds has garnered significant interest lately due to their wide range of applications and rapid advancement. The structural flexibility and optical properties of these organic–inorganic hybrid compounds are determined by organic cations,[1,2] while the inorganic anions govern their thermal and mechanical properties. These materials are receiving increasing attention due to their unique ability to selectively harness the benefits of both organic and inorganic materials, creating diverse and exceptional materials.

The development of ferroelastic semiconductors is hindered by the significant challenge associated with fabricating hybrid perovskites.[3] Moreover, the successful incorporation of ferroelectric properties in hybrid perovskites renders them ideal for application in flexible wearable devices.[4,5] Organic–inorganic hybrid compounds utilizing $CH_3NH_3PbX_3$ (X = Cl, Br, or I) have demonstrated successful applications in solar cells.[6–8] Nonetheless, the toxic nature of Pb in these perovskites and its susceptibility to decomposition in humid air necessitates the exploration of environmentally friendly alternatives. A class of environmentally friendly free-Pb hybrid organic–inorganic compounds, $[NH_3(CH_2)_nNH_3]MX_4$ ($n$ = 2, 3, 4, …; M = Co, Zn, Mn, Cd, Fe, Cu; X = Cl, Br), has emerged.[9–14] These compounds are characterized by organic $[NH_3(CH_2)_nNH_3]$ cations arranged along the longest axis, with inorganic $MX_4$ anions positioned between them. The physical and chemical properties of the organic–inorganic hybrid perovskites depend on the characteristics of the organic cations, the geometry of the inorganic anions (metal halide ions; $(MX_6)^{2-}$ or $(MX_4)^{2-}$), and reaction stoichiometry. When M is Mn, Cu, or Cd, the structure comprises alternating corner-shared octahedral $(MX_6)^{2-}$ units with organic layers. However, in the case of M = Co or Zn, the structures consist of tetrahedral $(MX_4)^{2-}$ units sandwiched between layers of organic cations.[15–24] Recently, researches of $[NH_3(CH_2)_nNH_3]BX_2X'_2$ with different halogen ions were reported by Abdel-Aal *et al.*[25–27] The organic and inorganic layers form infinite 0D or 2D structures, connected by N–H···Cl hydrogen bonds.[28–31] In particular, the structural rearrangements due to changes along the length of cations are also very important factors.

One interesting hybrid compound is 1,6-hexanediammonium tetrachlorozincate (II), ($[NH_3(CH_2)_6NH_3]ZnCl_4$), which contains a $[NH_3(CH_2)_6NH_3]$ cation and a $ZnCl_4$ anion, and has phase transition temperatures of 289 K, 342 K, and 385 K as measured

[a]Graduate School of Carbon Convergence Engineering, Jeonju University, Jeonju 55069, Korea

[b]Department of Science Education, Jeonju University, Jeonju 55069, Korea. E-mail: aeranlim@hanmail.net; arlim@jj.ac.kr

[c]Korea Basic Science Institute, Seoul Western Centre, Seoul 03759, South Korea

[d]Department of Chemistry, Kyungpook National University, Daegu 41566, South Korea

† Electronic supplementary information (ESI) available. CCDC 2278866, 2302890 and 2302891. See DOI: https://doi.org/10.1039/d3ra05752f

© 2023 The Author(s). Published by the Royal Society of Chemistry

Open Access Article. Published on 26 October 2023. Downloaded on 10/1/2024 11:16:26 AM. This article is licensed under a Creative Commons Attribution-NonCommercial 3.0 Unported Licence.

by differential scanning calorimetry (DSC). The structure of the $[NH_3(CH_2)_6NH_3]ZnCl_4$ crystal at room temperature is triclinic with unit cell parameters of $a$ = 7.2816 Å, $b$ = 10.0996 Å, $c$ = 10.0972 Å, $\alpha = 74.368°$, $\beta = 88.046°$, $\gamma = 85.974°$, and $Z = 2$.[32] The terminal ammonium ions of the $[NH_3(CH_2)_6NH_3]$ cation are connected by hydrogen bonds with the Cl ions (*i.e.*, N–H···Cl) in the $ZnCl_4$ anion.

The growth and structures of $[NH_3(CH_2)_nNH_3]ZnCl_4$ ($n$ = 2–5) single crystals along the length of cations have been previously confirmed by X-ray diffraction analyses.[19,33–36] The thermal stabilities and spin–lattice relaxation times with temperature change were mainly utilized to study the physicochemical properties and structural dynamics of the single crystals.[35–38] Despite the numerous applications of these compounds, there has been limited discussion regarding the thermal properties and structural dynamics attributed to variations in the methylene chain length.

In this study, organic–inorganic hybrid $[NH_3(CH_2)_6NH_3]ZnCl_4$ single crystals replacing with eco-friendly were grown using the aqueous solution method, and their crystal structures, phase transition temperatures ($T_C$), and thermal properties were studied. The effect of temperature on coordination geometry, which can provide valuable insights into the physical and chemical properties of compounds, was discussed based on information obtained from $^1$H, $^{13}$C, and $^{14}$N nuclear magnetic resonance (NMR) chemical shifts. The energy transfer was investigated by employing the spin–lattice relaxation time ($T_{1\rho}$). Moreover, the interplay of N–H···Cl hydrogen bonds connecting the organic cation and inorganic anion was considered. The results of this study demonstrated comparability and provided explanations for research on structural dynamics of $[NH_3(CH_2)_nNH_3]ZnCl_4$ ($n$ = 2, 3, 4, 5, and 6) where the methylene length chain length varies as a parameter.

## 2. Experimental

$[NH_3(CH_2)_6NH_3]ZnCl_4$ single crystals were grown by the slow evaporation method at 300 K after dissolving $NH_2(CH_2)_6NH_2 \cdot 2HCl$ (Aldrich, 99%) and $ZnCl_2$ (Aldrich, 98%) in a ratio of 1 : 1 in distilled water. The single crystal grown here had a size of about 7 mm × 3 mm × 2 mm and was colorless and transparent.

The lattice constants at 250, 300, and 350 K were obtained by single-crystal X-ray diffraction (SCXRD) at the Seoul Western Center of the Korea Basic Science Institute (KBSI). Single crystal experiments were performed using a Bruker diffractometer (D8 Venture PHOTON III M14) with Mo-Kα radiation source and a nitrogen cold flow (−50 °C). Data collection was obtained using SMART APEX3 (Bruker 2016) and SAINT (Bruker, 2016) software. The structure was analyzed by full-matrix least-squares on $F^2$ using SHELXTL.[39] All hydrogen atoms were represented in geometric positions. Additionally, powder X-ray diffraction (PXRD) patterns were obtained at various temperatures using an XRD system equipped with a Mo-Kα as the same target used in SCXRD.

Differential scanning calorimetry experiments (TA, DSC 25) were performed at temperatures ranging from 193 to 573 K at a heating rate of 10 °C min$^{-1}$ under $N_2$ gas.

Thermogravimetry analysis (TGA) and differential thermal analysis (DTA) measurements were conducted from 300 to 873 K under $N_2$ gas at a heating rate of 10 °C min$^{-1}$ using a thermogravimetric analyzer (TA Instrument).

Temperature-dependences for NMR spectra and spin-lattice relaxation times ($T_{1\rho}$) were measured using a 400 MHz (AVANCE III HD) solid-state NMR spectrometer (Bruker, Germany) in the same laboratory as above. The Larmor frequency for the $^1$H magic angle spinning (MAS) NMR experiment was 400.13 MHz, and TMS (tetramethylsilane) was used as the standard material to accurately measure the $^1$H NMR chemical shifts. The Larmor frequency for the $^{13}$C MAS NMR experiment was 100.619 MHz, and adamantane was used as the standard material for measuring the $^{13}$C NMR chemical shifts. Static $^{14}$N NMR chemical shifts were measured using the one-pulse method at a Larmor frequency of 28.90 MHz, and $NH_4NO_3$ was used as the reference material. Meanwhile, the spin–lattice relaxation time $T_{1\rho}$ values were measured using a $\pi/2$–$\tau$ pulse by a spin-lock pulse of duration $\tau$, where the pulse width of $\pi/2$ for $^1$H and $^{13}$C were 4.0 and 3.6 μs, respectively. The spinning rate to minimize the sideband of the NMR signal was 10 kHz. $N_2$ gas flow and heater current were used to adjust and maintain the desired temperature.

## 3. Results and discussion

### 3.1 Single-crystal XRD measurements

The single-crystal XRD patterns of $[NH_3(CH_2)_6NH_3]ZnCl_4$ were obtained at 250, 300, and 350 K. The SCXRD result at three temperatures showed a triclinic system with $P1$ (bar) space group and the cell constants of $a$ = 7.2844 (2) Å, $b$ = 10.1024 (3) Å, $c$ = 10.1051 (3) Å, $\alpha$ = 74.3060 (10)°, $\beta$ = 85.9270 (10)°, $\gamma$ = 88.0170 (10)°, and $Z$ = 2 at 300 K. These results were in good agreement with data at 300 K reported by Mostafa and El-khiyami.[32] On the other hand, the structures and lattice parameters were unchanged at 250, 300, and 350 K, as shown in Table 1, and it between 300 K and 350 K does not change to be significantly at the phase transition temperature of 340 K previously reported.[32] Fig. 1 shows the structure of the $[NH_3(CH_2)_6NH_3]$ cation and $ZnCl_4$ anion, the atomic numbering scheme, and the thermal ellipsoids of the H atoms in the $[NH_3(CH_2)_6NH_3]ZnCl_4$ crystal. In $ZnCl_4$, the Zn atom is surrounded by four Cl atoms, forming a tetrahedron. Infinite chains consisting of face-shared $ZnCl_4$ tetrahedra and four doubly bridging chloride ions link the adjacent Zn centers. This crystal is characterized by the N–H···Cl hydrogen bonds, connecting the cation to the anion. Bond lengths for Zn–Cl, N–C, C–C, C–H, N–H at three temperatures, are shown in Table 2. At 250 and 300 K, three N–H···Cl hydrogen bonds were formed, however, one N–H···Cl was broken at 350 K, and two N–H···Cl hydrogen bonds remained. The CIF files results of SCXRD for the crystal structures at 250, 300, and 350 K are shown in the ESI (1, 2, and 3†).

### 3.2 Phase transitions and powder XRD measurements

The phase transition temperature of the $[NH_3(CH_2)_6NH_3]ZnCl_4$ crystal was investigated using a DSC experiment which involved

 © 2023 The Author(s). Published by the Royal Society of Chemistry

Open Access Article. Published on 26 October 2023. Downloaded on 10/1/2024 11:16:26 AM.
This article is licensed under a Creative Commons Attribution-NonCommercial 3.0 Unported Licence.

Table 1 Crystal data and structure refinement for $[NH_3(CH_2)_6NH_3]ZnCl_4$ at 250 K, 300 K, and 350 K

| Temperature | 250 K | 300 K | 350 K |
|---|---|---|---|
| Chemical formula | $C_6H_{18}N_2ZnCl_4$ | $C_6H_{18}N_2ZnCl_4$ | $C_6H_{18}N_2ZnCl_4$ |
| Weight | 325.39 | 325.39 | 325.39 |
| Crystal system | Triclinic | Triclinic | Triclinic |
| Space group | *P*1 (bar) | *P*1 (bar) | *P*1 (bar) |
| *a* (Å) | 7.2757 (4) | 7.2844 (2) | 7.2972 (3) |
| *b* (Å) | 10.0165 (6) | 10.1024 (3) | 10.1542 (4) |
| *c* (Å) | 10.0348 (6) | 10.1051 (3) | 10.1812 (3) |
| *α* (°) | 75.028 (2) | 74.3060 (10) | 73.8420 (10) |
| *β* (°) | 86.496 (2) | 85.9270 (10) | 87.9390 (10) |
| *γ* (°) | 88.354 (2) | 88.0170 (10) | 85.6380 (10) |
| *Z* | 2 | 2 | 2 |
| *V* (Å$^3$) | 705.10 (7) | 714.01 (4) | 722.41 (5) |
| Radiation type | Mo-Kα | Mo-Kα | Mo-Kα |
| Wavelength (Å) | 0.71073 | 0.71073 | 0.71073 |
| Reflections collected | 14 848 | 26 702 | 27 217 |
| Independent reflections | 3539 ($R_{int} = 0.0242$) | 3538 ($R_{int} = 0.0272$) | 3595 ($R_{int} = 0.0295$) |
| Goodness-of-fit on $F^2$ | 1.039 | 1.042 | 1.021 |
| Final *R* indices [$I > 2$ sigma($I$)] | $R_1 = 0.0283$, w$R_2 = 0.0687$ | $R_1 = 0.0359$, w$R_2 = 0.0964$ | $R_1 = 0.0446$, w$R_2 = 0.1405$ |
| *R* indices (all data) | $R_1 = 0.0369$, w$R_2 = 0.0740$ | $R_1 = 0.0480$, w$R_2 = 0.1046$ | $R_1 = 0.0656$, w$R_2 = 0.1613$ |

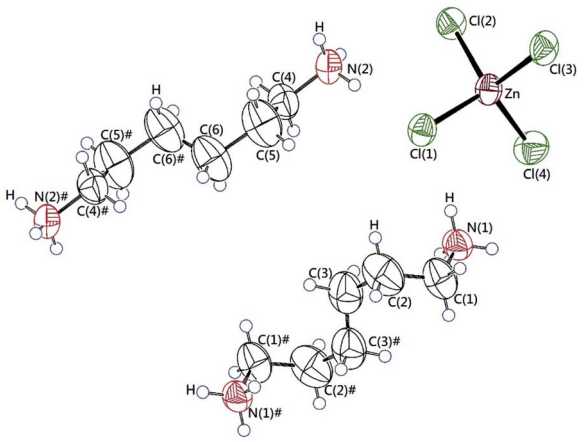


Fig. 1 The thermal ellipsoid plots for $[NH_3(CH_2)_6NH_3]ZnCl_4$ crystal structure at 300 K.

Table 2 The bond lengths (Å) of $[NH_3(CH_2)_6NH_3]_2ZnCl_4$ at 250 K, 300 K, and 350 K

| Temperature | 250 K | 300 K | 350 K |
|---|---|---|---|
| Zn–Cl (1) | 2.2454 (7) | 2.2795 (8) | 2.2749 (10) |
| Zn–Cl (2) | 2.2787 (6) | 2.2776 (8) | 2.2765 (11) |
| Zn–Cl (3) | 2.2828 (6) | 2.2686 (8) | 2.2449 (12) |
| Zn–Cl (4) | 2.2691 (6) | 2.2442 (9) | 2.2707 (11) |
| N (1)–C (1) | 1.480 (3) | 1.479 (4) | 1.458 (6) |
| N (2)–C (4) | 1.487 (3) | 1.467 (4) | 1.466 (6) |
| C (1)–C (2) | 1.479 (4) | 1.482 (6) | 1.365 (9) |
| C (2)–C (3) | 1.556 (4) | 1.578 (7) | 1.585 (11) |
| C (3)–C (3)# | 1.496 (6) | 1.454 (9) | 1.476 (19) |
| C (4)–C (5) | 1.507 (4) | 1.435 (6) | 1.431 (10) |
| C (5)–C (6) | 1.547 (4) | 1.584 (7) | 1.620 (12) |
| C (6)–C (6)# | 1.498 (6) | 1.465 (11) | 1.399 (15) |
| C–H | 0.980 | 0.970 | 0.970 |
| N–H | 0.900 | 0.890 | 0.890 |
| N (1)–H (1)–Cl (2) | | 3.287 | |
| N (2)–H (2)–Cl (2) | | 3.479 | |
| N (2)–H (2)–Cl (4) | | 3.738 | |

heating the crystal from 200 K to 550 K at a rate of 10 °C min$^{-1}$, with a sample size of 8.8 mg. The DSC curve, shown in Fig. 2, revealed the presence of two weak endothermic peaks at 340 K and 408 K, respectively, along with a strong endothermic peak at 473 K. The endotherm peak at 340 K was relatively small, making it challenging to accurately measure the enthalpy. However, at 408 K and 473 K, the enthalpy values of 796 J mol$^{-1}$ and 21 kJ mol$^{-1}$ were obtained, respectively. The temperature-induced variations in the single crystal were examined using an optical polarization microscope to accurately confirm the three peaks seen in DSC. It was observed that the crystal exhibited minimal changes in the temperature range of 300–450 K, and melting of the single crystal began at near 470 K (*i.e.*, $T_m = 470$ K) as shown in the inset of Fig. 2.

The temperature-dependent PXRD experiment was conducted, and the corresponding results are presented in Fig. 3, covering a range of 8–60° (2$\theta$). The PXRD patterns below 400 K,

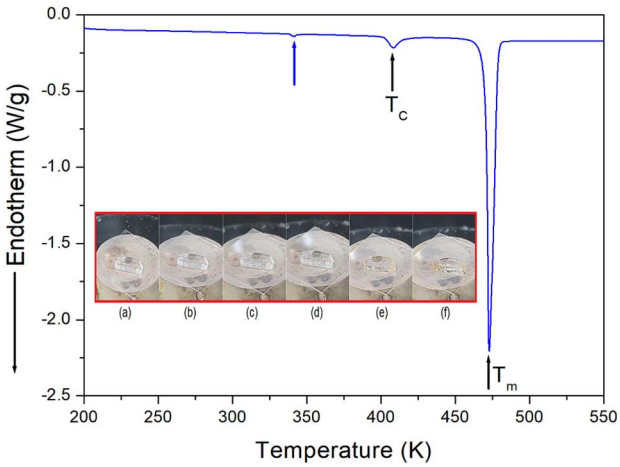


Fig. 2 Differential scanning calorimetry (DSC) curve of $[NH_3(CH_2)_6NH_3]ZnCl_4$ (inset: changes in the crystal at various temperatures: (a) 300 K, (b) 370 K, (c) 420 K, (d) 440 K, (e) 470 K, and (f) 490 K).

Open Access Article. Published on 26 October 2023. Downloaded on 10/1/2024 11:16:26 AM.
This article is licensed under a Creative Commons Attribution-NonCommercial 3.0 Unported Licence.

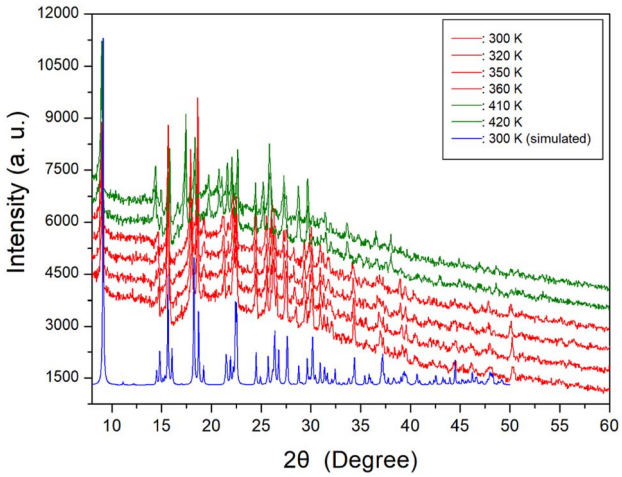


Fig. 3 Powder X-ray diffraction (PXRD) patterns at various temperatures, and the blue color is simulated PXRD pattern at 300 K.

indicated by red color, exhibited slight differences compared to those recorded at 410 K, represented by the olive color. This difference was attributed to $T_C$ (= 408 K). Notably, the PXRD results were well consistent with the DSC findings. The PXRD patterns did not exhibit any changes corresponding to the small endothermic peak near 340 K observed in the DSC analysis. Also, the triclinic structure derived from SCXRD results at 300 K and 350 K remained unchanged. And, the simulated XRD pattern based on the CIF file at 300 K is shown is represented in Fig. 3, and this result agrees well with the pattern obtained from PXRD experiment.

Therefore, the phase transition temperature ($T_C$) determined from DSC, PXRD, SCXRD, and optical polarizing microscopy experiments, was found to be 408 K. These results were not consistent with the previously reported values of 289 K, 342 K, and 385 K.[32]

### 3.3 Thermal properties

To understand the thermal characteristics, the $[NH_3(CH_2)_6NH_3]ZnCl_4$ crystal were assessed through TGA and DTA experiments at the heating rate of 10 °C min$^{-1}$ with a method similar to that of the DSC experiment. As shown in Fig. 4, the endothermic peak at 408 K in the DSC curve of Fig. 2 is very small, so there is almost no change in the TGA and DTA curves. In other words, it shows thermal stability near the phase transition temperature of 408 K. And, the DTA curve exhibited a peak around 474 K, which correlates with the melting temperature determined from the DSC and optical polarizing microscope analyses. The TGA and DTA results indicated that the crystal displayed thermal stability up to approximately 584 K, referred to as the partial thermal decomposition temperature ($T_d$). Beyond this temperature, $[NH_3(CH_2)_6NH_3]ZnCl_4$ experienced weight loss, and the amount of solid residue was determined using the molecular weight. The weight loss rapidly declined between 600 and 800 K, and approximately 22% weight loss occurred near 636 K due to the decomposition of 2HCl. Around 800 K, a weight loss of 90% was observed, resulting from the decomposition of $NH_2(CH_2)_6NH_2 \cdot 2HCl$, leaving behind only the inorganic $ZnCl_2$ anions.[40]

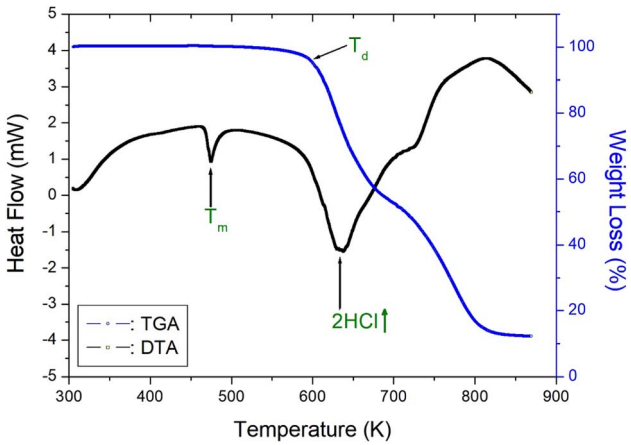


Fig. 4 Thermogravimetry analysis and differential thermal analysis curves of $[NH_3(CH_2)_6NH_3]ZnCl_4$.

### 3.4 $^1$H and $^{13}$C MAS NMR spectra

The $^1$H MAS NMR spectra of the $[NH_3(CH_2)_6NH_3]ZnCl_4$ crystal were acquired *in situ* as a function of temperature, and the corresponding $^1$H chemical shifts are shown in Fig. 5. The TMS reference signal was used as the standard for $^1$H chemical shifts. At lower temperatures, a single resonance signal with an asymmetric shape was observed, resulting from the overlapping $^1$H resonance lines of $NH_3$ and $CH_2$ in the organic $[NH_3(CH_2)_6NH_3]$ cations. The left (A) and right (B) sides of the resonance signal exhibited unequal half-full width at half maximum (FWHM). At 158 K, a single resonance line was detected at a chemical shift of 6.07 ppm. With increasing the temperature

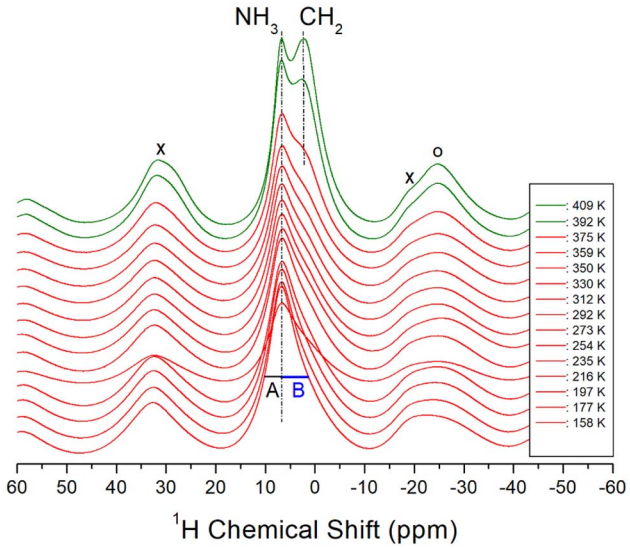


Fig. 5 $^1$H MAS NMR chemical shifts for $NH_3$ and $CH_2$ in $[NH_3(CH_2)_6NH_3]ZnCl_4$ as a function of temperature, and the spinning rate is 10 kHz. The cross (×) and open circle (○) indicate the sidebands for $NH_3$ and $CH_2$, respectively. A and B show the half-full width at half maximum for $NH_3$ and $CH_2$.

 © 2023 The Author(s). Published by the Royal Society of Chemistry

Open Access Article. Published on 26 October 2023. Downloaded on 10/1/2024 11:16:26 AM.
This article is licensed under a Creative Commons Attribution-NonCommercial 3.0 Unported Licence.

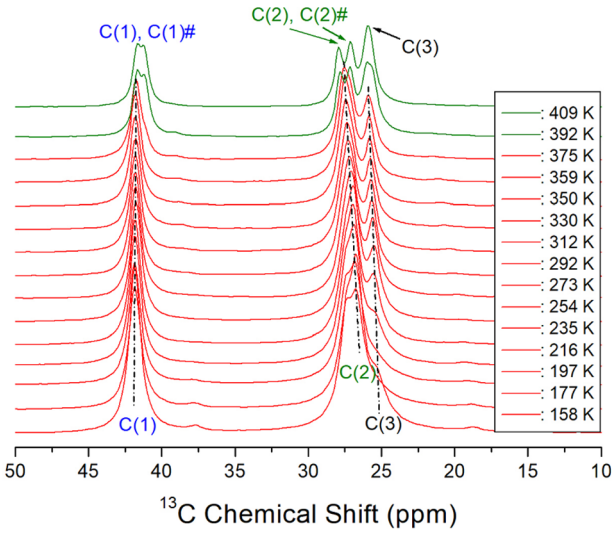


Fig. 6 $^{13}$C MAS NMR chemical shifts for C (1), C (1)#, C (2), C (2)#, and C (3) in $[NH_3(CH_2)_6NH_3]ZnCl_4$ as a function of temperature, and the spinning rate is 10 kHz.

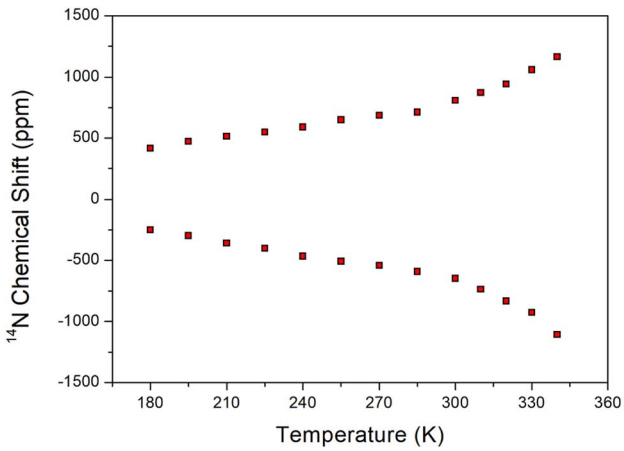


Fig. 7 Static $^{14}$N NMR chemical shifts of $[NH_3(CH_2)_6NH_3]ZnCl_4$ single crystal as a function of temperature.

to 410 K, the NMR line displayed a separation into two distinct resonance lines at chemical shifts of 6.79 and 2.13 ppm for $NH_3$ and $CH_2$, respectively. The $NH_3$ spinning sidebands are marked with crosses, and the sidebands for $CH_2$ are marked with open circles in Fig. 5. Above 392 K, near $T_C$, the $^1$H NMR signals for $NH_3$ and $CH_2$ began to separate. In addition, the narrow line width of the left signal (*i.e.*, $NH_3$) and the broader line width of the right signal (*i.e.*, $CH_2$) aligned well with the respective number of $^1$H in the $NH_3$ and $CH_2$ groups. The $^1$H chemical shifts for $NH_3$ remained almost unchanged as the temperature increased, whereas those of $CH_2$ experienced changes. These observations suggest that the surrounding environments of $^1$H of the $NH_3$ changes little and that of the $CH_2$ changes slightly.

The variations of $^{13}$C chemical shifts in the MAS NMR spectra with temperature are shown in Fig. 6. The adamantane reference signal was used as the standard for the $^{13}$C chemical shifts. In the $[NH_3(CH_2)_6NH_3]$ cation illustrated in Fig. 1, the $CH_2$ groups positioned adjacent to the $NH_3$ are designated as C (1) and C (1)#, while the centrally located $CH_2$ groups are denoted as C (3) and C (3)#. The $CH_2$ groups situated between C (1) and C (3) are labeled as C (2) and C (2)#, respectively. At 292 K, three distinct $^{13}$C NMR signals were observed; C (1) at 41.76 ppm, C (2) at 27.23 ppm, and C (3) at 25.71 ppm. As the temperature increased, the chemical shifts of C (1) remained largely unchanged, while those of C (2) and C (3) shifted positively. Near the $T_C$ temperature, C (1) was resolved into C (1)# with a different environment, and C (2) was separated into C (2) # with a different environment. No notable changes were observed in C (1), C (2), and C (3) around 340 K. And, the difference of the chemical shift between (2) and C (2)# is larger than that between C (1) and C (1)#. Separation into C (1) and C (1)# and C (2) and C (2)# above $T_C$ means that the symmetry of cations above $T_C$ is lowered.

### 3.5 $^{14}$N static NMR spectrum

The $^{14}$N static NMR spectrum of $[NH_3(CH_2)_6NH_3]ZnCl_4$ single crystal was obtained in the temperature range of 180–420 K (Fig. 7). The $^{14}$N chemical shift range exhibited a significantly wider span compared to the $^1$H chemical shift range, making it valuable for determining the surrounding environment of $^{14}$N. In this study, the external magnetic field was measured in an arbitrary direction of the single crystal. Considering the spin number of $^{14}$N as $I = 1$, the NMR spectrum predicts two resonance lines due to the quadrupole interaction.[41] However, due to the very low Larmor frequency of 28.90 MHz for obtaining the $^{14}$N NMR spectrum, the signal acquisition was challenging. The $^{14}$N NMR chemical shifts shown in Fig. 7 disappeared above 340 K. The SCXRD results listed in Table 2 indicated the formation of three N–H···Cl hydrogen bonds at 250 and 300 K. However, one N–H···Cl at 350 K was broken, leaving two N–H···Cl hydrogen bonds intact. This observation aligned with the disappearance of the $^{14}$N NMR signal above 340 K. The continuous change in the $^{14}$N chemical shifts with increasing temperature indicated a variation in the local environment and coordination geometry of the $^{14}$N atoms.

### 3.6 $^1$H and $^{13}$C spin–lattice relaxation times

The spin–lattice relaxation time $T_{1\rho}$ for $^1$H and $^{13}$C was determined by acquiring an FID after applying the spin-lock pulse. The intensity changes of the measured magnetization are described by the following equation:[42]

$$S(t)/S(0) = \exp(-\tau/T_{1\rho}), \quad (1)$$

where $S(t)$ is the intensity of the resonance line at the delay time $t$, $S(0)$ is the intensity of the NMR spectrum at the delay time $t = 0$. The experiment was conducted with various $\tau$ values, and the corresponding $T_{1\rho}$ values were determined from the slopes of the resulting intensities plotted against the delay time according to eqn (1). The $T_{1\rho}$ values of the $^1$H of $NH_3$ and $CH_2$ in $[NH_3(CH_2)_6NH_3]ZnCl_4$ were obtained, and are represented in

Open Access Article. Published on 26 October 2023. Downloaded on 10/1/2024 11:16:26 AM. This article is licensed under a Creative Commons Attribution-NonCommercial 3.0 Unported Licence.

Fig. 8 as a function of the 1000/temperature. The $T_{1\rho}$ value for $^1$H in $NH_3$ and $CH_2$ decreased slightly with increasing temperature, followed by a rapid increase above 177 K. Moreover, the $^1$H $T_{1\rho}$ values in $NH_3$ and $CH_2$ reached a maximum near 340 K, followed by a subsequent decrease in a similar manner. At 177 K, the minimum $T_{1\rho}$ value for $^1$H in $CH_2$ and $NH_3$ were 4.6 ms and 6.2 ms, respectively. These patterns in $T_{1\rho}$ values indicate active molecular motion. According to the Bloembergen–Pound–Purcell (BPP) theory,[43,44] the experimental $T_{1\rho}$ value is directly related to the correlation time $\tau_C$ as shown in eqn (2).

$$\begin{aligned}(T_{1\rho})^{-1} &= R[4f_1(\omega_1) + f_2(\omega_C - \omega_H) + 3f_3(\omega_C) \\ &\quad + 6f_4(\omega_C + \omega_H) + 6f_5(\omega_H)], \\ f_1 &= \tau_C/[1 + \omega_1{}^2\tau_C{}^2], \\ f_2 &= \tau_C/[1 + (\omega_C - \omega_H)^2\tau_C{}^2], \\ f_3 &= \tau_C/[1 + \omega_C{}^2\tau_C{}^2], \\ f_4 &= \tau_C/[1 + (\omega_C + \omega_H)^2\tau_C{}^2], \\ f_5 &= \tau_C/[1 + \omega_H{}^2\tau_C{}^2], \end{aligned} \tag{2}$$

where $R$ $(\gamma_H\ \gamma_C\ \hbar/r^3)^2$; constant, $\omega_1$; the spin-lock field, and $\omega_C$ and $\omega_H$; the Larmor frequencies for carbon and proton. When $\omega_1\tau_C = 1$, a minimum value is obtained for $T_{1\rho}$, enabling the determination of the constant $R$ using $\tau_C$. $R$, $\omega_1$, $\omega_H$, $\omega_C$, and $T_{1\rho}$ are then used to calculate $\tau_C$ at a given temperature change. Local field fluctuations around $^1$H can be explained by the thermal motion of thermally activated protons. For the correlation time $\tau_C$, the activation energy $E_a$ can be obtained using eqn (3) shown below [41]

$$\tau_C = \tau_C\ (0)\ \exp(-E_a/k_B T) \tag{3}$$

where $\tau_C$ (0); the pre-correlation time, $E_a$; the activation energy, $k_B$; the Boltzmann constant, and $T$; the temperature. The magnitude of $E_a$ is related to molecular kinetics. When 1000/T for $^1$H is plotted against $\tau_C$ on a logarithmic scale, as shown in Fig. 8, $E_a$ values of 16.82 ± 1.71 kJ mol$^{-1}$ and 19.61 ± 1.71 kJ mol$^{-1}$ for $^1$H in $NH_3$ and for $^1$H in $CH_2$ can be obtained

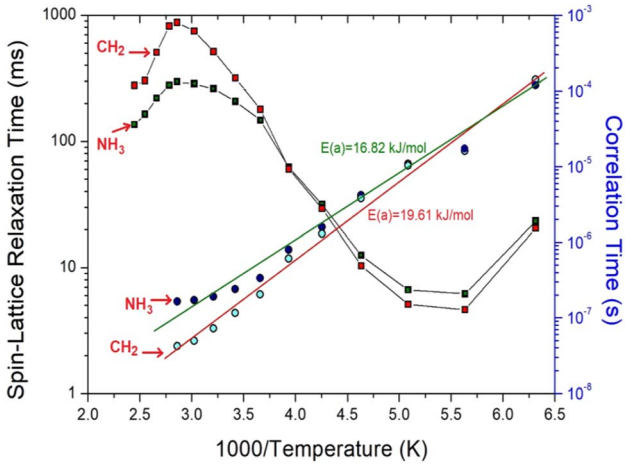


Fig. 8 $^1$H spin–lattice relaxation times $T_{1\rho}$ and correlation times $\tau_C$ for $NH_3$ and $CH_2$ in $[NH_3(CH_2)_6NH_3]ZnCl_4$ as a function of 1000/temperature. The solid lines represent the $^1$H activation energies ($E_a$) in $NH_3$ and $CH_2$.

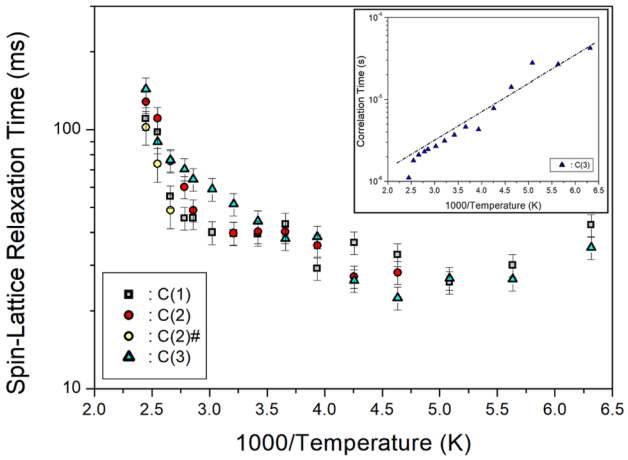


Fig. 9 $^{13}$C spin–lattice relaxation times $T_{1\rho}$ for C (1), C (2), C (2)#, and C (3) of $[NH_3(CH_2)_6NH_3]ZnCl_4$ as a function of 1000/temperature (inset: correlation time $\tau_C$ for C (3) as a function of 1000/temperature).

from the slopes of the solid lines, which were almost similar within the error range.

Furthermore, the $T_{1\rho}$ values of C (1), C (2), C (2)#, and C (3) for $^{13}$C in $[NH_3(CH_2)_6NH_3]ZnCl_4$ were measured, and their results are represented in Fig. 9 as a function of the 1000/temperature. The $T_{1\rho}$ values for $^{13}$C of all three types kinds exhibited a slight decrease as the temperature rose and showed a slow increase at temperatures above 216 K. Notably, the $T_{1\rho}$ values of C (1), C (2), C (2)#, and C (3) demonstrated trends similar to each other. Regarding the $T_{1\rho}$ value of $^1$H, C (3) exhibits a minimum value of 22 ms, and their $^{13}$C $T_{1\rho}$ patterns underwent active molecular motion. The logarithmic plot of the $\tau_C$ *versus* 1000/T for $^{13}$C is shown as an inset in Fig. 9. The slope of the dotted line in the figure yielded $E_a = 6.56 \pm 0.63$ kJ mol$^{-1}$, and the values for C (1), C (2), and C (2)# were nearly identical within the margin of error.

### 3.7 $[NH_3(CH_2)_nNH_3]ZnCl_4$ ($n$ = 2, 3, 4, 5, and 6) crystals

We then conducted a comparison between our study on $[NH_3(CH_2)_nNH_3]ZnCl_4$ ($n = 6$) and previous studies on $n = 2$, 3, 4, and 5.[35–38] The structures, space groups, and lattice constants of $[NH_3(CH_2)_nNH_3]ZnCl_4$ ($n$ = 2, 3, 4, 5, and 6) crystals were shown in Table 3. Correspondingly, the crystal structure was found to be monoclinic for odd values of $n$, triclinic for even values of $n$, and orthorhombic for $n = 2$. By analyzing the physicochemical properties of these organic–inorganic compounds, we examined the impact of the methylene chain length. With an increase in the length of the methylene chain, the thermal stability is enhanced, and it is related to intermolecular forces. This trend is clearly illustrated in Fig. 10, where the results showed an increase to 534, 549, 559, 581, and 584 K for $n$ = 2, 3, 4, 5, and 6, respectively. The changes of $T_d$ can be considered as electronic configuration; the 3d electron of the M shell is filled, and the valence electron is 4s$^2$.

On another note, as $n$ increased, the $^1$H $T_{1\rho}$ below 300 K became shorter, while the behavior of $T_{1\rho}$ above 300 K varied, as shown in Fig. 11. Similarly, Fig. 12 illustrates the overall

 © 2023 The Author(s). Published by the Royal Society of Chemistry

Open Access Article. Published on 26 October 2023. Downloaded on 10/1/2024 11:16:26 AM.
This article is licensed under a Creative Commons Attribution-NonCommercial 3.0 Unported Licence.

Table 3 The structures, space groups, and lattice constants (Å) of $[NH_3(CH_2)_nNH_3]ZnCl_4$ ($n$ = 2, 3, 4, 5, and 6) crystals

| $n$ | 2 | 3 | 4 | 5 | 6 |
|---|---|---|---|---|---|
| Structure | Orthorhombic | Monoclinic | Triclinic | Monoclinic | Triclinic |
| Space group | $P2_12_12_1$ | $P2_1/n$ | $P1$ (bar) | $C2/c$ | $P1$ (bar) |
| Lattice constant | | | | | |
| $a$ (Å) | 8.832 | 10.670 | 7.2839 | 21.4175 | 7.2844 |
| $b$ (Å) | 9.811 | 10.576 | 8.1354 | 7.3574 | 10.1024 |
| $c$ (Å) | 11.089 | 10.755 | 10.4592 | 19.1079 | 10.1051 |
| $\alpha$ (°) | | | 77.6527 | | 74.3060 |
| $\beta$ (°) | | 118.477 | 80.3358 | 120.5190 | 85.9270 |
| $\gamma$ (°) | | | 82.8355 | | 88.0170 |
| $Z$ | 4 | 4 | 2 | 8 | 2 |
| Ref. | 33 | 31 and 34 | 35 | 36 | 32, present |

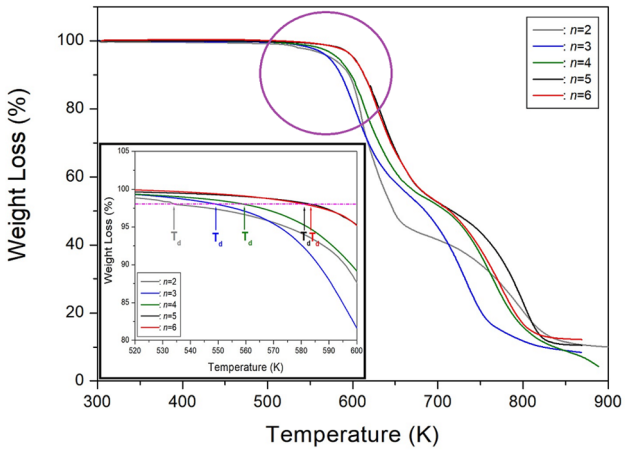


Fig. 10 Thermogravimetry analysis (TGA) curves of $[NH_3(CH_2)_nNH_3]ZnCl_4$ ($n$ = 2, 3, 4, 5, and 6) according to the methylene chain length.

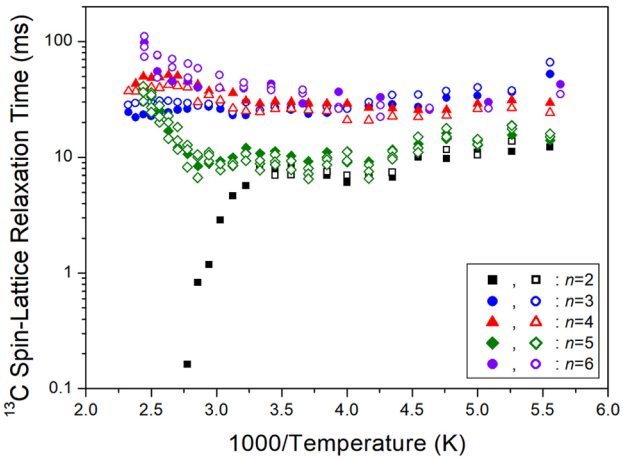


Fig. 12 $^{13}C$ spin–lattice relaxation times $T_{1\rho}$ of $[NH_3(CH_2)_nNH_3]ZnCl_4$ ($n$ = 2, 3, 4, 5, and 6) for different methylene chain lengths as a function of 1000/temperature.

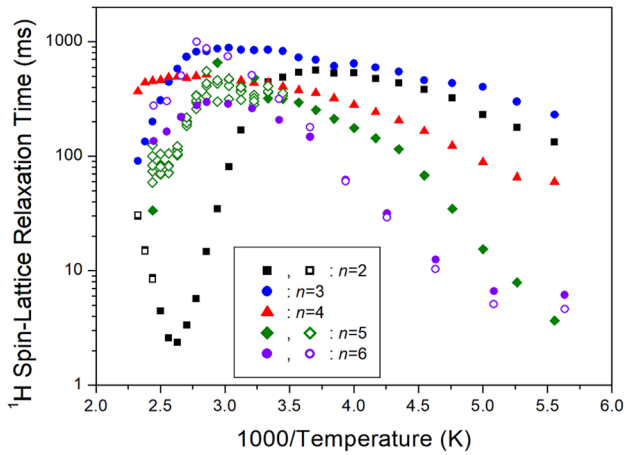


Fig. 11 $^{1}H$ spin–lattice relaxation times $T_{1\rho}$ of $[NH_3(CH_2)_nNH_3]ZnCl_4$ ($n$ = 2, 3, 4, 5, and 6) for various methylene chain lengths as a function of 1000/temperature.

temperature-dependent behavior of $^{13}C$ $T_{1\rho}$. The substantial difference between $^{13}C$ $T_{1\rho}$ (10 times less) and $^{1}H$ $T_{1\rho}$ indicates that energy transfer for $^{13}C$ is more efficient. However, when $n$ is 2, both $^{1}H$ and $^{13}C$ $T_{1\rho}$ displayed different characteristics compared to when $n$ = 3, 4, 5, and 6. Furthermore, the length of the chain (*i.e.*, $n$) did not distinctly affect the temperature dependence of $^{1}H$ and $^{13}C$ $T_{1\rho}$, but it increased the temperature dependence of $T_d$.

## 4. Conclusion

Studying the physical properties of $[NH_3(CH_2)_6NH_3]ZnCl_4$ crystals is essential for their practical application. In this study, we successfully grew these crystals with triclinic structures. Through comprehensive examinations utilizing DSC, SCXRD, and PXRD, we established that the phase transition temperature of these crystals occurred at 408 K. Remarkably, this phase transition temperature was different from those observed in other groups, indicating that slight differences in crystal growth conditions may be the underlying cause.

Additionally, exceptionally high thermal stability was observed, with the crystals exhibiting remarkable stable up to approximately 584 K. The NMR analyses of the $[NH_3(CH_2)_6NH_3]ZnCl_4$ crystal showed that the chemical shifts caused by the local field surrounding $^{1}H$, $^{13}C$, and $^{14}N$ of the cation and

Open Access Article. Published on 26 October 2023. Downloaded on 10/1/2024 11:16:26 AM. This article is licensed under a Creative Commons Attribution-NonCommercial 3.0 Unported Licence.

anion as the temperature increases, and the surrounding environment of their atoms also changes. Based on the temperature-dependent chemical, it was found that the coordination geometry around $^{1}H$ and $^{13}C$ exhibited high symmetry below $T_C$, whereas it showed low symmetry above $T_C$. The structural analysis using SCXRD revealed no changes in the structure below 350 K. However, at 250 and 300 K, three N–H···Cl hydrogen bonds were identified. At 350 K, one N–H···Cl hydrogen broke, leaving two intact. This finding appears to be connected to the significant change observed in the $^{14}N$ chemical shifts. The variations in the N–H···Cl hydrogen bond arises from alterations in the coordination geometry of $Cl^-$ around $Zn^{2+}$ in the $ZnCl_4$ anion. Notably, the activation energy of $^{1}H$ was three times higher than that of $^{13}C$, suggesting that the energy transfer of $^{13}C$ is smaller than that of $^{1}H$.

As a result, the effect of cation length can be attributed to an increase in the decomposition temperature $T_d$ by the intermolecular forces. These findings suggest that the characteristics of the $CH_2$ chain length hold promise for potential future applications.

## Author contributions

A. R. Lim performed X-ray experiments, and wrote the manuscript. S. H. Kim measured NMR experiments.

## Conflicts of interest

There are no conflicts to declare.

## Acknowledgements

This work was supported by the national Research Foundation of Korea (NRF) grant funded by the Korea government (MSIT) (2023R1A2C2006333). This research was also supported by the Basic Science Research Program through the National Research Foundation of Korea (NRF), funded by the Ministry of Education, Science, and Technology (2016R1A6A1A03012069).

## References

1 W. Zang and R.-G. Xiong, *Chem. Rev.*, 2012, **112**, 1163.
2 A. R. Lim and S. H. Kim, *ACS Omega*, 2021, **6**, 27568.
3 C. Su, M. Lun, Y. Chen, Y. Zhou, Z. Zhang, M. Chen, P. Huang, P. D. Fu and Y. Zhang, *CCS Chem.*, 2022, **4**, 2009.
4 Y. Xie, Y. Ai, Y.-L. Zeng, W.-H. He, X.-Q. Huang, D.-W. Fu, J.-X. Gao, X.-G. Chen and Y.-Y. Tang, *J. Am. Chem. Soc.*, 2020, **142**, 12486.
5 D.-W. Fu, J.-X. Gao, W.-H. He, X.-Q. Huang, Y.-H. Liu and Y. Ai, *Angew. Chem., Int. Ed.*, 2020, **59**, 17477.
6 S. K. Abdel-Aal, A. S. Abdel-Rahman, G. G. Kocher-Oberlehner, A. Ionov and R. Mozhchil, *Acta Crystallogr., Sect. A: Found. Adv.*, 2017, **70**, C1116.
7 Y. Liu, L. Collins, R. Proksch, S. Kim, B. R. Watson, B. Doughty, T. R. Calhoun, M. Ahmadi, A. V. levlev, S. Jesse, S. T. Retterer, A. Belianinov, K. Xiao, J. Huang, B. G. Sumpter, S. V. Kalinin, B. Hu and O. S. Ovchinnikova, *Nat. Mater.*, 2018, **17**, 1013.
8 J. Lee, W. Lee, K. Kang, T. Lee and S. K. Lee, *Chem. Mater.*, 2021, **33**, 370.
9 C. Sourisseau, G. Lucazeau and A. J. Dianoux, *J. Phys.*, 1983, **44**, 967.
10 K. Chhor, J. F. Bocquet and C. Pommier, *J. Chem. Thermodyn.*, 1985, **17**, 379.
11 V. V. Eremenko, V. I. Fomin and V. S. Kurnosov, *Phys. B*, 1994, **194–196**, 187.
12 J.-C. Bissey, N. Filloleau, N.-B. Chanh, R. Berger and S. Flandrois, *Solid State Commun.*, 1998, **106**, 385.
13 M. M. Bogdan, M. I. Kobets and E. N. Khats'ko, *Low Temp. Phys.*, 1999, **25**, 192.
14 S. J. Lee, M. Y. Choi and A. R. Lim, *ACS Omega*, 2021, **6**, 15392.
15 N. Narita and I. Yamada, *J. Phys. Soc. Jpn.*, 1996, **65**, 4054.
16 D. B. Mitzi, K. Chondroudis and C. R. Kagan, *IBM J. Res. Dev.*, 2001, **45**, 29.
17 H. Manaka, I. Yamada and T. Goto, *J. Phys. Soc. Jpn.*, 2002, **71**, 2822.
18 Y. Wei, P. Audebert, L. Galmiche, J. S. Lauret and E. Deleporte, *Materials*, 2014, **7**, 4789.
19 D. B. Mitzi, *J. Chem. Soc., Dalton Trans.*, 2001, **1**, 1.
20 S. Ahmad, C. Hanmandlu, P. K. Kanaujia and G. Vijaya Prakash, *Opt. Mater. Express*, 2014, **4**, 1313.
21 I. Saikumar, S. Ahmad, J. J. Baumberg and G. Vijaya Prakash, *Scr. Mater.*, 2012, **67**, 834.
22 K. Pradeesh, G. S. Yadav, M. Singh and G. Vijaya Prakash, *Mater. Chem. Phys.*, 2010, **124**, 44.
23 K. Pradeesh, J. Baumberg and G. Vijaya Prakash, *Appl. Phys. Lett.*, 2009, **95**, 173305.
24 S. K. Abdel-Aal and A. S. Abdel-Rahman, *J. Cryst. Growth*, 2017, **457**, 282.
25 S. K. Abdel-Aal and A. Ouasri, *J. Mol. Struct.*, 2022, **1251**, 131997.
26 S. K. Abdel-Aal, M. F. Kandeel, A. F. El-Sherif and A. S. Abdel-Rahman, *Phys. Status Solidi A*, 2021, **218**, 2100136.
27 S. K. Abdel-Aal, A. S. Abdel-Rahman, W. M. Gamal, M. Abdel-Kader, H. S. Ayoub, A. F. El-Sherif, M. F. Kandeel, S. Bozhko, E. E. Yakimov and E. B. Yakimov, *Acta Crystallogr., Sect. B: Struct. Sci., Cryst. Eng. Mater.*, 2019, **75**, 880.
28 S. K. Abdel-Aal, G. Kocher-Oberlehner, A. Ionov and R. N. Mozhchil, *Appl. Phys. A*, 2017, **123**, 531.
29 W. Liu, J. Xing, J. Zhao, X. Wen, K. Wang, P. Lu and Q. Xiong, *Adv. Opt. Mater.*, 2017, **5**, 1601045.
30 J.-C. Bissey, N. Filloleau, N.-B. Chanh, R. Berger and S. Flandrois, *Solid State Commun.*, 1998, **106**, 385.
31 A. R. Lim, S. H. Kim and Y. L. Joo, *Sci. Rep.*, 2021, **11**, 8408.
32 M. F. Mostafa and S. S. El-khiyami, *J. Solid State Chem.*, 2014, **209**, 82.
33 W. T. A. Harrison, *Acta Crystallogr., Sect. E: Struct. Rep. Online*, 2005, **61**, m1951–m1952.
34 A. Kallel, J. Fail, H. Fuess and A. Daoud, *Acta Crystallogr., Sect. B: Struct. Crystallogr. Cryst. Chem.*, 1980, **36**, 2788.
35 A. R. Lim, *RSC Adv.*, 2021, **11**, 37824.
36 A. R. Lim and J. Cho, *Sci. Rep.*, 2022, **12**, 16901.

 © 2023 The Author(s). Published by the Royal Society of Chemistry

Open Access Article. Published on 26 October 2023. Downloaded on 10/1/2024 11:16:26 AM.
This article is licensed under a Creative Commons Attribution-NonCommercial 3.0 Unported Licence.

37 A. R. Lim, *ACS Omega*, 2020, **5**, 31417.
38 A. R. Lim, S. H. Kim and Y. L. Joo, *Sci. Rep.*, 2021, **11**, 8408.
39 *SHELXTL v6.10*, Bruker AXS, Inc., Madison, Wisconsin, USA, 2000.
40 A. R. Lim and S. H. Kim, *ACS Omega*, 2021, **6**, 27568.
41 A. Abragam, *The Principles of Nuclear Magnetism*, Oxford University press, 1961.
42 J. L. Koenig, *Spectroscopy of Polymers*, Elsevier, 1999.
43 N. Bloembergen, E. M. Purcell and R. V. Pound, *Phys. Rev.*, 1948, **73**, 679.
44 R. K. Harris, *Nuclear Magnetic Resonance Spectroscopy*, Pitman Pub, 1983.